

Deep Learning of Aftershock Hysteresis Effect Based on Elastic Dislocation Theory

Jin Chen^{1,2}, Hong Tang^{1,2}, and Wenkai Chen³

¹ Key Laboratory of Environmental Change and Natural Disaster of Ministry of Education, Faculty of Geographical Science, Beijing Normal University, Beijing 100875, China

² State Key Laboratory of Remote Sensing Science, Faculty of Geographical Science, Beijing Normal University, Beijing 100875, P.R. China

³ Institute of Lanzhou Earthquake Research, China Earthquake Administration, Gansu Lanzhou 730000, China

Correspondence to: Hong Tang (tanghong@bnu.edu.cn)

Abstract: This paper selects fault source models of typical earthquakes across the globe and uses a volume extending 100 km horizontally from each mainshock rupture plane and 50 km vertically as the primary area of earthquake influence for calculation and analysis. A deep neural network is constructed to model the relationship between elastic stress tensor components and aftershock state at multiple time scales, and the model is evaluated. Finally, based on the aftershock hysteresis model, the aftershock hysteresis effect of the Wenchuan earthquake in 2008 and Tohoku earthquake in 2011 is analyzed, and the aftershock hysteresis effect at different depths is compared and analyzed. The correlation between the aftershock hysteresis effect and the Omori formula is also discussed and analyzed. The constructed aftershock hysteresis model has a good fit to the data and can predict the aftershock pattern at multiple time scales after a large earthquake. Compared with the traditional aftershock spatial analysis method, the model is more effective and fully considers the distribution of actual faults, instead of treating the earthquake as a point source. The expansion rate of the aftershock pattern is negatively correlated with time, and the aftershock patterns at all time scales are roughly similar and anisotropic.

Key Words: Okada dislocation theory; FCNN; aftershock hysteresis effect; aftershock pattern; the Omori formula.

38 1 Introduction

39 After the occurrence of strong earthquakes, there are often a large number of aftershocks, which
40 constitute the aftershock sequence. The aftershocks can lead to new damage to the area damaged by the main
41 earthquake. Therefore, it is necessary to study aftershocks and stimulate further discussion. Stein et al.
42 systematically discussed the influence of the static stress of the main earthquake on the spatial distribution
43 of aftershocks (Stein et al., 1983). A large number of earthquake examples show that the change in Coulomb
44 stress produced by the main earthquake is greater than 0.01 Mpa, which readily triggers aftershocks (Ma et
45 al., 2005; Toda, 2003; Harris, 1998). In addition to the Coulomb failure stress change method, the deep
46 learning method is a new emerging method that can address some questions of physical mechanism. The
47 prediction of the aftershock sequence based on the stress state of the crustal medium is also problematic and
48 is a focus of source physics. The neural network has the characteristics of a black box, which can avoid the
49 complicated physical mechanisms when predicting the aftershock pattern (Brodi, 2001; Moustira et al., 2011).
50 In 2018, Phoebe et al. proposed a deep neural network to study the spatial distribution of aftershocks
51 following the main earthquake. A neural network classifier based on stress variation was designed by the
52 author to determine the possibility of a spatial distribution of aftershocks (Phoebe et al., 2018). This idea
53 combines traditional physical analysis mechanisms with data-driven machine learning mechanisms, which
54 can improve our understanding of the complex physical mechanism of earthquakes. Kong et al. also analyzed
55 its necessity (Kong et al., 2019).

56 The distribution of aftershocks is not only related to spatial change but also to temporal change, which
57 may be related to the actual properties of the medium, i.e., the viscoelastic medium and the porous two-phase
58 medium are closer to the actual geological medium than the elastic medium. The hysteresis effect of the
59 viscoelastic medium on stress change, the effect of readjustment of pore fluid on stress change and other
60 time-dependent medium properties are equally important to post-earthquake stress change, which is an issue
61 that is receiving increasing attention in post-earthquake effects research. In the study of the propagation of a
62 seismic wave and its focal mechanism, the earth medium is assumed to be a completely elastic body. Prior
63 to the main earthquake, the crustal medium will be continuously deformed due to the long-term and slow
64 action of tectonic stress. In the process of stress accumulation, the strain energy of the crustal medium will
65 accumulate continuously and be stored in the crust in the form of elastic strain energy. When the stress
66 intensity is greater than the bearing stress intensity in the crust, the crust will lose its stability and form the
67 main earthquake fracture surface, which will produce the main earthquake. Simultaneously, the elastic strain
68 energy stored in the crust will be released suddenly. After the occurrence of the main earthquake, the source
69 body and its surrounding medium will return to a steady state. However, because the main earthquake causes
70 a sudden change in the stress state of the medium, the accumulated elastic strain energy in the entire stress
71 field cannot be released completely at one time, and it will continue to accumulate in other areas, and it will
72 ultimately be released in the form of an aftershock sequence. Therefore, there is a hysteresis effect between
73 the aftershock and the main earthquake (Gu et al., 1979). Omori and Utsu proposed the time distribution
74 formulas of aftershocks. However, the formulas are based on statistical significance, which cannot reflect the
75 underlying reason for the change in aftershock distribution over time, and cannot spatialize the temporal
76 change in aftershocks (Omori, 1894; Utsu, 1961). Many scholars also analyzed the temporal-spatial
77 distribution characteristics of aftershocks by building a model. For example, the ETAS model proposed by
78 Ogata (Ogata, 1988), the KJ model proposed by Kagan et al. (Kagan et al., 1994), and the model improved
79 by Ogata based on ETAS (Ogata, 1998). In 2009, Wong et al. proposed a joint distribution model that
80 parameterized the aftershock location based on the distance and relative angle between aftershocks and
81 mainshocks (Wong et al., 2009). The above temporal-spatial models of aftershocks are all based on point-
82 source earthquakes, while the actual earthquake sources are faults. So the distribution of the main fault zone
83 should be considered when predicting the aftershock pattern. Some spatial models also ignore the relative
84 angle or distance between mainshock and aftershocks. These deficiencies are taken into account when
85 building the new prediction model.

86 In this paper, a method based on deep neural networks is proposed to analyze the probability distribution
87 of aftershocks following the main earthquake on multiple time scales, which indirectly reflects the hysteresis
88 effect of aftershocks at different positions under the stress field of the main earthquake. The SRCMOD fault
89 source model database and earthquake events are used as raw data. First, the analysis area of each main
90 earthquake is gridded, and then the aftershocks of each main earthquake are entered into the grids. The DC3D
91 displacement model is used to calculate the components of stress change tensor for each cell. Based on this
92 grid, the results of the calculation are used as the input to train the neural network, and the aftershock
93 hysteresis model is then obtained. As the application analysis cases for the model, the Wenchuan earthquake
94 and the Tohoku earthquake are not included in the training set or the validation set. Finally, the spatial
95 distribution and expansion characteristics of the aftershock hysteresis model are obtained for both horizontal
96 and vertical directions. In addition, we focus on two important concepts, namely “hysteresis effect” and
97 “aftershock pattern”. The “hysteresis effect” refers to the change in spatial distribution of aftershocks with
98 the change of time scale. The “aftershock pattern” refers to the spatial distribution of aftershocks at a certain
99 time.

100 2 Data and Methods

101 2.1 Data

102 2.1.1 Raw data

103 Two types of data are used in this paper, SRCMOD finite fault data and the ISC (International
104 Seismological Centre) seismic catalogue.

105 The inversion of finite fault source data facilitates a better understanding of the complexity of the
106 earthquake rupture process. Although the spatial resolution of the model is low, it can provide information
107 on deep seismic slip and fault evolution over time. Therefore, the finite fault model is an important means to
108 further study the mechanics and kinematics of the process of earthquake fracture. The online SRCMOD
109 database provides the inversion results for many typical earthquakes from 1906 to present. These results are
110 uploaded by seismologists globally after the main earthquake through inversion. Because the earth's crust is
111 used as an elastic medium in the calculation of coseismic displacement stress, we don't consider the impact
112 of the background of each earthquake. There are 19 finite fault source models used in this analysis: 15 are
113 used as training data and 4 are used as validation data.

114 The aftershocks following each main earthquake are obtained from the international earthquake center
115 (ISC). For the main earthquake examples in this paper, the aftershocks within 1 d, 30 d, 90 d, 180 d, and 365
116 d and within a volume extending 100 km horizontally from each mainshock rupture plane and 50 km vertically
117 are used for analysis of the aftershock sequences.

118 2.1.2 Data processing

119 After acquiring the limited fault source data and aftershock sequence data, it is necessary to process
120 them to create the final data for analysis. First, the volume extending 100 km horizontally from each
121 mainshock rupture plane and 50 km vertically is divided into a grid of 5 km³ cubes. Five time scales of
122 aftershock sequence data are then entered into each cube. The aftershock state of a cell with an aftershock is
123 defined as 1 and that of a cell without an aftershock is defined as 0. The final training data has 15 aftershock
124 sequences containing 318,210 subcells, and the validation data has 4 aftershock sequences containing 89,900
125 subcells.

127 2.2.1 Okada elastic dislocation theory

128 The inversion analysis of seismogenic faults after earthquakes is a popular topic in seismology, and in
 129 the process of inversion, the application of dislocation theory and models is essential. The dislocation model
 130 was first used to analyze fault movement in 1958 (Steketee, 1958). Steketee introduced dislocation theory
 131 into the study of seismic deformation fields, and described the relationship between discontinuous
 132 displacement on the dislocation plane and the displacement field in an isotropic medium. Okada summarized
 133 the existing research in 1985 and proposed a formula for the calculation of displacement in an isotropic,
 134 uniform elastic half space. This formula can be used to calculate the coseismic deformation caused by any
 135 fault in the elastic half space (Okada, 1985; Okada, 1992). Okada dislocation theory systematically
 136 summarizes the relationship between point source dislocation and surface deformation caused by rectangular
 137 dislocation. The crustal movement is typically slow, and the crustal medium generally shows viscosity and
 138 plasticity over a long time scale. At present, Okada dislocation theory is the most widely used dislocation
 139 theory and is often used in combination with InSAR technology. InSAR is used to monitor the surface
 140 coseismic deformation field, and Okada theory is then used to conduct fault slip inversion (Shan et al., 2017;
 141 Wang et al., 2018; Zhao, 2019; Cheng et al., 2019).

142 Therefore, Okada elastic dislocation theory is used to calculate the coseismic strain stress field of the
 143 main earthquake in the paper. The Okada elastic dislocation model, which ignores the influence of
 144 stratification in the earth's medium, is widely used in the study of coseismic deformation of the seismic signal
 145 source. Okada gives the analytical expression of the partial derivative $\frac{\partial u_i}{\partial x_j}$ ($i, j = 1, 2, 3$) of the displacement \mathbf{u}
 146 of the finite fault plane in the elastic half space (Okada, 1992). This expression is used to obtain the strain
 147 tensor $\boldsymbol{\varepsilon}$ as

$$\varepsilon_{ij} = \frac{1}{2} \left(\frac{\partial u_i}{\partial x_j} + \frac{\partial u_j}{\partial x_i} \right)$$

148 and the Lamé constant in the linear solid medium is used to obtain the surrounding stress change tensor $\boldsymbol{\sigma}$ as

$$\sigma = \begin{bmatrix} \lambda \text{tr}[\boldsymbol{\varepsilon}] + 2\mu\varepsilon_{xx} & 2\mu\varepsilon_{xy} & 2\mu\varepsilon_{xz} \\ 2\mu\varepsilon_{yx} & \lambda \text{tr}[\boldsymbol{\varepsilon}] + 2\mu\varepsilon_{yy} & 2\mu\varepsilon_{yz} \\ 2\mu\varepsilon_{zx} & 2\mu\varepsilon_{zy} & \lambda \text{tr}[\boldsymbol{\varepsilon}] + 2\mu\varepsilon_{zz} \end{bmatrix}$$

149 where λ and μ are Lamé constants. In this paper, the crustal medium is regarded as a Poisson body, and the
 150 two Lamé coefficients are both 3.0×10^{10} Pa. The parameter $\text{tr}[\boldsymbol{\varepsilon}]$ is the trace of strain tensor $\boldsymbol{\varepsilon}$.

153 2.2.2 FCNN

154 To analyze the hysteresis effect of aftershocks, it is necessary to establish a model that can predict the
 155 damage modes of aftershocks at multiple time scales. We constructed a fully connected deep neural network
 156 to simulate the relationship between the change value of the elastic stress tensor and aftershock and to explain
 157 the hysteresis effect of aftershocks. The network established here is a network with six hidden layers. Except
 158 for the second hidden layer, which has 100 neurons, the other five hidden layers have 50 neurons. The input
 159 layer dimension of the entire network is 12, its input eigenvalue is the combination of the absolute value
 160 of six independent components of the elastic stress at the center of each subunit and the negative number of
 161 the absolute value, for a total of 12 inputs.

162 Then we analyze the correlation between aftershocks and stress change, which is closely related to the
 163 inputs of FCNN. At present, the research on aftershocks is primarily based on statistical methods, and the
 164 research content primarily focuses on the distribution of aftershock strength and time attenuation. The
 165 intensity distribution of aftershocks follows the G-R relationship $M = a - bM$, where M is the magnitude,
 166 N is the number of aftershocks with magnitude greater than or equal to M , and a and b are the scale
 167 coefficient. The value of b generally varies from 0.6 to 1.1 (Utsu, 2002), and its value is related to the

168 regional stress state (Scholz, 1968; Megi, 1962). A low b value is related to a high stress background, i.e.,
169 the b value is relatively low during strong aftershock activity (Yi et al., 2011).

170 The study of time attenuation of aftershocks begins with the statistical description of frequency
171 attenuation characteristics of the aftershock sequence using the Omori formula (Omori, 1894). In 1961, Utsu
172 et al. proposed that the frequency attenuation rate of the actual aftershock sequence is faster than that
173 calculated by the Omori formula (Utsu, 1961) and proposed the modified Omori formula $n(t) = K(t + c)^{-p}$,
174 where $n(t)$ is the aftershock frequency per unit time, c is a constant, and p is the attenuation coefficient of the
175 aftershock sequence. For a large number of aftershock sequences, the modified Omori formula accurately
176 describes the time attenuation of aftershocks. In the modified Omori formula, the c value is related to the
177 incomplete recording time after the main earthquake (Kagan et al., 2005), which can provide a physical
178 explanation for the aftershock attenuation after the main earthquake (Lindman et al., 2005). This value is also
179 related to the rupture mode of the main earthquake (Narteau et al., 2009), i.e., the aftershock attenuation is
180 affected by the stress state and related to the stress change.

181 The stress change caused by the main earthquake can be calculated by the Coulomb fracture stress
182 change, which is also the most widely used analytical method at present. The change in Coulomb stress
183 produced by the main earthquake will trigger the stress of the following aftershocks (Harris, 1998). Some
184 seismologists believe that if the change in Coulomb fracture stress is positive around the main earthquake, it
185 will promote fault movement and trigger aftershocks; if the change in Coulomb fracture stress is negative, it
186 will inhibit fault movement, and the probability of triggering an aftershock is reduced (Lin, 2004; Harris,
187 1998; Han, 2003). According to the research of DeVries et al., the Coulomb fracture stress change is an
188 inadequate explanation for aftershocks, and the relationship between the positive and negative values of stress
189 change and the triggering of aftershocks requires further exploration. DeVries et al. modeled the relationship
190 between stress change and aftershock triggering by training a neural network (DeVries et al., 2018). The
191 variation in Coulomb fracture stress depends on the geometric properties and coseismic dislocations of the
192 source fault (King et al., 1994; Zhu et al., 2009). Therefore, the change value of the stress tensor, which is
193 closely related to the dislocation of the same earthquake, can be used as the aftershock variable to build the
194 model.

195 In addition, Meade and DeVries et al. tested many stress-related indicators in 2017 to explain the
196 influence of the coseismic stress field of the main earthquake on the location of aftershocks. Their results
197 show that the sum of the absolute values of the six independent components of the stress tensor, the von
198 Mises yield criterion and the maximum shear stress produce the best interpretation, and these variables can
199 be obtained by the combination of the absolute values of the six independent components of the stress tensor
200 and the negative values of the absolute values. Therefore, these variables are also used as the network input
201 (Meade et al., 2017; Mignan et al., 2019). The input components are expressed as $|\sigma_{xx}|$, $|\sigma_{xy}|$, $|\sigma_{xz}|$, $|\sigma_{yy}|$,
202 $|\sigma_{yz}|$, $|\sigma_{zz}|$, $-|\sigma_{xx}|$, $-|\sigma_{xy}|$, $-|\sigma_{xz}|$, $-|\sigma_{yy}|$, $-|\sigma_{yz}|$, and $-|\sigma_{zz}|$. The dimension of the network output
203 layer is 1, and the output value is the relative probability of aftershocks in each cell, which is between 0 and
204 1. The dropout layer is also set after each hidden layer. The dropout layer is set to alleviate the occurrence of
205 over-fitting in the model training process, which can have a regularization effect. In addition, the activation
206 function of each hidden layer in the network is a Relu function, and the optimizer is Adadelta. The activation
207 function of the output layer is a sigmoid function, which maps variables between 0 and 1 (Figure 1). Five
208 scales are analyzed in this paper. Five neural networks are constructed to train five submodels. Each
209 submodel is independent from the others and does not affect the others.

210 2.2.3 Model evaluation metric

211 The ROC curve and the AUC are used to evaluate the model. The AUC (area under curve) is defined as
212 the area enclosed by the coordinate axis under the ROC curve, and the value of the area cannot be greater
213 than 1. Because the ROC curve is generally located above the straight line $y = x$, the AUC value range is
214 between 0.5 and 1. Based on the AUC value, we can interpret the accuracy of the classifier. When $AUC = 1$,
215 the classifier is essentially a perfect classifier, whereas when $AUC = 0.5$, the classifier is making a random

216 assessment and the obtained model is nonsensical. For the training samples in this paper, there is a class
217 imbalance between positive and negative samples. A characteristic of the ROC curve is that when the
218 distribution of positive and negative samples in the test set changes, the ROC curve can remain unchanged.
219 The closer the ROC curve is to the Y-axis and $y = 1$, i.e., the higher the AUC value of the classifier, the
220 greater the classification accuracy. Generally, when the AUC is less than 0.6, the accuracy of the classifier is
221 poor; when the AUC is less than 0.75, the accuracy of the classifier is moderate; and when the AUC is greater
222 than 0.75, the accuracy of the classifier is good. The output of the model in this paper is a probability value
223 between 0 and 1. When the ROC curve is used to evaluate the model, it is conducted at five time scales, and
224 the model under each time scale is evaluated as a two-classification problem.

225 3 Results

226 3.1 Evaluation of the aftershock hysteresis model

227 The aftershock hysteresis model under multiple time scales is obtained by using the neural network to
228 train the constructed training dataset. In this paper, five submodels are trained, and the final hysteresis model
229 is composed of five submodels. The output value of the neural network in each cell is binarized with a
230 threshold value of 0.5. A cell with a predicted value greater than 0.5 is assigned as 1, and a cell with a
231 predicted value less than 0.5 is assigned as 0. Based on the trained aftershock hysteresis model, the aftershock
232 patterns are predicted for the Wenchuan earthquake at multiple time scales, and the ROC curves are obtained
233 for the different time scales. The AUC values of the five time scales are all above 0.8, both the training and
234 validation sets, and some are close to 0.9. The AUC values of the training set are all higher than those of the
235 validation set for the different time scales. The neural network designed by Phoebe et al. is used for aftershock
236 prediction. The AUC value of the training model on the validation set is 0.849 (Figure 2). In this paper, the
237 AUC value of each submodel on the validation set is similar to the research results of Phoebe et al. therefore,
238 the model achieves good prediction results at different time scales.

239 For comparison, we forecast the aftershock location based on the static Coulomb failure stress change.
240 Considering the influence of shear stress, normal stress and friction coefficient on the active fault plane,
241 Coulomb failure stress change (ΔCFS) can be expressed as

$$242 \Delta CFS = \Delta\tau + \mu\Delta\sigma$$

243 where μ is apparent friction coefficient, $\Delta\sigma$ is the normal stress on the fault plane and $\Delta\tau$ is shear stress in the
244 direction of fault slip. Based on previous studies, the friction coefficient in this paper is 0.4 (King et al., 1994;
245 Wan et al., 2004). Numerous studies have shown that aftershocks will occur when ΔCFS is greater than
246 $+0.01\text{Mpa}$. In order to compare and analyze the output of FCNN, we need to transform the ΔCFS to 0~1.
247 Similar to the last layer of FCNN, the variation function adopts a variant of the sigmoid function as follows

$$248 \Delta CFS' = \frac{1}{(1 + e^{-10(\Delta CFS - 0.01)})}$$

249 where $\Delta CFS'$ represents the Coulomb failure stress change after sigmoid transformation. We know that the
250 traditional sigmoid function is similar to the jump function. In the analysis process of this paper, 0.01Mpa is
251 the threshold value to determine whether aftershocks are generated, so the parameter 0.01 in the formula is
252 the translation coefficient, that is, the traditional sigmoid function shifts 0.01Mpa to the right. Parameter 10
253 is the zoom coefficient, which compresses the sigmoid function horizontally to make its shape approach the
254 jump function as much as possible. When ΔCFS is greater than 0.01Mpa, $\Delta CFS'$ approaches 1 as much as
255 possible, and when ΔCFS is less than 0.01Mpa, $\Delta CFS'$ approaches 0 as much as possible. Then we evaluated
256 the results and calculated the AUC value on each time scale by ROC curve. Compared with the results of the
257 previous model, the AUC results obtained by the method based on static Coulomb failure stress change are
258 generally poor, which are no more than 0.6 (Figure 3).

260 3.2.1 Aftershock hysteresis failure mode

261 According to the tectonic stress figure of the Wenchuan earthquake, the Wenchuan earthquake was
 262 located in the Longmenshan area in the border mountains east of the Qinghai Tibetan Plateau. The geological
 263 structure in this area is complex. The main Longmenshan fault zone is composed of a series of roughly
 264 parallel thrust faults. It is divided into a front mountain zone and a back mountain zone with the Yingxiu-
 265 Beichuan central fault as the boundary. From Northwest to Southeast, the main fault zone consists of the
 266 back mountain fault, the central fault and the front mountain fault. The main fault forming the Wenchuan
 267 earthquake is the Yingxiu-Beichuan central fault. According to the beachball plot of the focal mechanism
 268 solution in Figure 4, the strong aftershocks following the Wenchuan earthquake are ~~primarily reverse faults~~
 269 ~~or thrust faults~~ under the action of compressive stress.

270 Based on the aftershock hysteresis model, the failure patterns of aftershocks are predicted at different
 271 time scales, and the section observation is conducted at ~~12,500 m~~ underground (essentially at the same depth
 272 as the source). Combined with the focal mechanism solution analysis of strong aftershocks around the main
 273 fault zone, the aftershocks in this area are mainly caused by the NW-trending and SE-trending crustal
 274 compressive stress (Figure 5). The expansion of the aftershock hysteresis pattern is observed, which is
 275 generally distributed along the fault strike and extends along the trend line of the main fault. Within one day
 276 after the main earthquake at Wenchuan, there were aftershocks over a wide area. The location of the
 277 aftershocks is distributed along the fault zone, and the location of the aftershocks is basically distributed in
 278 the geographical space predicted by the model.

279 Finally, the spatial results of the hysteresis effect of the Wenchuan earthquake are obtained by
 280 synthesizing the damage modes of the aftershocks at multiple time scales (Figure 6). The location of the
 281 aftershocks is basically along the main fault, i.e., the Yingxiu-Beichuan central fault. The model predicts that
 282 aftershocks are mainly distributed in Chengdu, Mianyang, Deyang, Guangyuan and Ngawa, which is
 283 consistent with the actual location of the aftershocks. Over time, the area of aftershocks expands outwards,
 284 and the rate ~~s~~ gradually. Using the main aftershock sequence from the Wenchuan earthquake as an
 285 example, the aftershock hysteresis patterns at different time scales are similar, and the direction of outward
 286 expansion is basically perpendicular to the distribution direction of the previous time scale. Compared with
 287 the attenuation map of earthquake intensity, the spatial distribution map of aftershock attenuation can provide
 288 some reference for follow-up disaster prevention and mitigation work after a large earthquake. We can further
 289 understand the attenuation law of aftershocks, and attempt to extend its time attenuation from a statistical
 290 perspective to a spatial perspective.

291 3.2.2 Aftershock hysteresis patterns at different depths

292 At different focal depths, the aftershock hysteresis patterns will also change. The focal depth range of
 293 the aftershocks analyzed in this paper is ~~0-20~~ km. The aftershock hysteresis effect is analyzed by selecting
 294 sections with depths of 2,500 m, 7,500 m, 12,500 m, 17,500 m, 22,500 m, 27,500 m, 32,500 m, 37,500 m
 295 and 42,500 m. Many previous studies have shown that the seismogenic layers in Central and western China
 296 are located in the middle and upper layers of the crust at a depth of no more than 20 km (Zhao et al., 1995;
 297 Yang et al., 2003). The aftershocks with a focal depth within 20 km are widely distributed (Figure 7). When
 298 the focal depth exceeds 20 km, the area where the aftershocks are generated suddenly decreases with
 299 increasing depth until no aftershocks are observed. The focal depth of the largest aftershock distribution range
 300 is 12500 m which is in the same range as the focal depth of the main earthquake. In the middle and upper
 301 layers of the earth's crust, the shapes of the aftershock hysteresis patterns are generally similar at different
 302 time scales. Over time, the shape of the aftershock hysteresis pattern generally expands outward in a similar
 303 pattern as the previous timescale. However, when the focal depth exceeds a certain value, the hysteresis
 304 pattern of the aftershocks substantially changes. In this case, when the focal depth is greater than 20 km, the
 305 area predicted for aftershocks significantly decreases, and the evolution of the hysteresis pattern is also

306 changed. Although the overall expansion direction is consistent with the main fault, the pattern is less regular
307 and more random.

308 3.3 Application of the model to the Tohoku earthquake in 2011

309 3.3.1 Aftershock hysteresis failure mode

310 Japan is located in the Circum-Pacific seismic belt at the intersection of the Eurasian plate and the Pacific
311 plate, which is an area with a frequent occurrence of global earthquakes. Due to the collision between the
312 Pacific plate and the Eurasian plate, the Pacific plate is subducted under the Eurasian plate, thus forming the
313 Japan Trench and the Japanese island arc. “OK” represents the Okhotsk plate, which is part of the Eurasian
314 plate, “PA” refers to the Pacific plate, and “PS” refers to the Philippine Sea plate, which is also part of the
315 Eurasian plate (Bird, 2003) (Figure 8). The epicenter of the earthquake was located in the subduction zone
316 of the Japanese trench. Based on the aftershock hysteresis model, the aftershock patterns within 1 d, 30 d, 90
317 d, 180 d and 365 d after the main earthquake are predicted, and the section (22.1 m) at the focal depth of
318 the main earthquake is selected for analysis. Using the Tohoku earthquake in Japan as an example, the
319 greatest expansion of the aftershock distribution area is observed within 30 d. The shape of the aftershock
320 patterns are similar at all time scales. The aftershock and the predicted aftershock patterns are distributed in
321 an approximately North-South direction along the Japan Trench and plate boundary.

322 The aftershock hysteresis model of the Tohoku earthquake is obtained by synthesizing the aftershock
323 patterns at different time scales (Figure 9). Over time, the expansion rate of the aftershock pattern gradually
324 slows down and the expansion direction is basically perpendicular to the aftershock pattern at the previous scale.
325 Most of the aftershocks of this earthquake occurred in the eastern Sea of Japan, and the concentrated area of
326 terrestrial aftershocks was located in Fukushima.

327 3.3.2 Aftershock hysteresis patterns at different depths

328 Similar to the Wenchuan earthquake, the aftershock hysteresis pattern of the Tohoku earthquake changes
329 with the change in depth. The magnitude of the earthquake was very large, reaching over $M_w 9$. The main
330 earthquake has a great impact on the surrounding area and the crust, which stores considerable energy, then
331 releases it in the form of aftershocks. The predicted expansion direction of the aftershock model is generally
332 consistent with that of the plate boundary and the Japan Trench. In this study, the maximum analysis depth
333 is 50 km. Using the depth section of the main shock source as the center, the actual aftershock pattern does
334 not change significantly when the depth change is small. This may be due to the large magnitude of the
335 earthquake. The area of the actual aftershock pattern is reduced at a depth of 42.1 m. However, the location
336 of the aftershock is still widely distributed. The expansion of the aftershock pattern also changes beginning
337 at a depth of 2750 m. The general direction of distribution is along the trench, and some areas begin to
338 expand vertically along the trench (Figure 10).

339 4 Discussion

340 4.1 Aftershock hysteresis effect

341 The modified Omori formula is $n(t) = K(t + c)^{-p}$, where $n(t)$ is the aftershock frequency per unit time,
342 and as t increases, $n(t)$ will decrease correspondingly to describe the time attenuation characteristics of
343 aftershocks. Compared with the Omori formula, the aftershock hysteresis effect analyzed in this paper can
344 be reflected by the correlation between the change of time scale and the region of aftershocks. Based on the
345 discussion of focal depth sections of the main earthquake, within one day after the Wenchuan earthquake,
346 the number of subunits with aftershocks is 213; within 30 d, it is 386, representing an increase of 81.6%;
347 within 90 d, it is 432, representing an increase of 11.9%; within 180 d, it is 466, representing an increase of
348 7.9%; and within 365 d, it is 488, representing an increase of 4.7%. Within one day after the Tohoku
349 earthquake, the number of subunits with aftershocks was 137; within 30 d, it was 595, representing an

350 increase of 334%; within 90 d, it was 724, representing an increase of 21.7%; within 180 d, it was 799,
351 representing an increase of 10.4%; and within 365 d, it was 856, representing an increase of 7.1%. The
352 aftershock pattern predicted by the model expands over time, but the expansion speed of the aftershock
353 pattern also gradually slows. The rate of expansion is most rapid 30 days after the earthquake. After 30 days,
354 the speed decreases significantly from 30 to 90 d. The aftershock pattern of the Wenchuan earthquake expanded
355 at a speed of 28.7 units/day within 30 d after the earthquake and then rapidly dropped to 7.8 units/day. The
356 aftershock pattern of the Tohoku earthquake in Japan expanded at a rate of 38.6 units/day within 30 d after
357 the earthquake and then dropped rapidly to 7.3 units/day. According to the correlation curve in Figure 11 and
358 Figure 12, the aftershock hysteresis effect is reflected by the expansion pattern of the aftershocks. Combined
359 with the comprehensive analysis of the previous two earthquake cases, the expansion rate of the aftershock
360 hysteresis effect is $v \propto n(t) \propto \frac{1}{t}$. Unlike previous research on the attenuation law of aftershocks based on
361 statistics (Narteau et al., 2005; Nanjo et al., 2007), this paper starts from another perspective, namely, spatial
362 distribution, and returns to the discussion of the attenuation law of aftershock spatial distribution.

363 4.2 Comparative analysis of prediction models

364 The widely used temporal-magnitude earthquake generation model (ETAS) was proposed by Ogata
365 (Ogata, 1988). Later on, he observed that the distribution of aftershock sequences tended to be elliptic rather
366 than circular. He established the anisotropic aftershock attenuation function and took the normal distribution
367 as the spatial distribution model of aftershock (Ogata, 1998). It is a widely observed fact that aftershocks
368 usually occur on or near the fault of mainshock. However, the normal distribution model does not include
369 the source mechanism information of the mainshock when predicting the aftershock mode. Kagan et al.
370 introduced the anisotropy function of the spatial smooth core into the long-term earthquake prediction, and
371 established the spatial smooth core model, including the source mechanism information of the mainshock
372 (Kagan et al., 1994). However, the above models ignore the internal relationship of the relative distance or
373 direction between the mainshock and the aftershocks. Based on this, Wong et al. proposed a joint distribution
374 model to parameterize the aftershock location according to the distance and relative angle between the
375 mainshock and aftershocks (Wong et al., 2009). In the prediction process of the above models, the epicentre
376 of the mainshock is used as a point source for analysis. Actually, the distribution of the fault plane of the
377 mainshock should be fully considered. Based on the finite fault model, the distribution information of the
378 main fault is considered in the paper. At the same time, the relative position and direction between the
379 mainshock and aftershocks have been considered in the process of calculating the variation of stress tensor
380 by using the Okada dislocation theory. Therefore, in the process of model training and learning, the relative
381 position relation is also learned. Compared with the static Coulomb failure stress change method, the
382 aftershock hysteresis model obtained has a better prediction effect.

383 In addition, the model is a six layer neural network, which is a black box model. Compared with the
384 traditional statistical model or physical model, is the deep learning model more complex? We think this
385 complexity is relative. In fact, the starting point of the traditional model and the model in this paper are
386 similar. They are all based on data, trying to find a relationship between some basic physical quantities and
387 aftershocks. The complexity of traditional models lies in the process of finding such a connection. The
388 complexity of deep learning model lies in its seemingly complex structure. The complex structure will lead
389 to the increase of the number of internal variables to be learned, and the rapid computing ability of today's
390 computers can solve this problem, so as to reduce manpower and time-consuming. In addition, the deep
391 learning model is a data-driven method. It will be more convenient than the traditional model when the data
392 set or the amount of data changes greatly or the model needs to be adjusted.

393 5 Conclusions

394 In this paper, based on the criterion of correlation between aftershocks and stress changes caused by the
395 main earthquakes, a deep neural network is trained using RCMOD finite fault data and the ISC seismic

396 catalogue and is used to construct an aftershock hysteresis model. Using the main aftershock sequences of
397 the Wenchuan earthquake and the Tohoku earthquake in Japan as examples, the characteristics of the
398 aftershock hysteresis effect in plane space and at different depths are then analyzed. The main contributions
399 are as follows:

400 (1) The trained model of aftershock hysteresis is accurate. It can predict the aftershock patterns at
401 multiple time scales after a large earthquake and produce a spatial distribution map of the aftershock
402 hysteresis effect. Compared with static Coulomb failure stress change, this model is more effective.

403 (2) Compared with the traditional aftershock spatial analysis method, the model fully considers the
404 distribution of actual faults in the prediction of aftershock pattern, instead of treating the earthquake as a
405 point source. In the analysis of the model, the relative position information between the mainshock and
406 aftershocks has been included.

407 (3) The expansion rate of the aftershock patterns changes over time, i.e., $v \propto n(t) \propto \frac{1}{t}$. In the middle
408 and upper layers of the crust, the shape of the aftershock pattern is generally consistent, and the expansion
409 direction is typically perpendicular to the direction of distribution of the previous time scale.

410 (4) According to the prediction results of the model, the aftershock patterns at all time scales are roughly
411 similar and anisotropic. The distribution law of aftershock hysteresis effect will change with the increase of
412 the depth.

413 In the analysis of each aftershock sequence, we only consider the influence of the main earthquake fault
414 zone. If we comprehensively consider the stress field superposition of multiple or all faults in the analysis
415 area of each earthquake case, the prediction of the aftershock pattern will be more accurate. In addition, we
416 focus on the location of the aftershocks and will further explore and study aftershocks from the perspectives
417 of magnitude and energy in the future.

418 Acknowledgments

419 The SRCMOD finite fault model data can be obtained from <http://equake-rc.info/srcmod/>. The ISC
420 earthquake events can be obtained from <http://www.isc.ac.uk/iscgem/>. The results of the aftershock hysteresis
421 effect are obtained by programming in Python, and some codes refer to previous research by Phoebe et al.
422 this study, the figures and the subsequent processing of the results are all performed using ArcGIS software.
423 This work was supported by the National Natural Science Foundation of China (No. 41971280) and the
424 National Key R&D Program of China (No. 2017YFB0504104).

425 Author Contributions

426 Conceptualization, H.T.; Funding acquisition, H.T.; Investigation, J.C.; Methodology, J.C. and H.T.;
427 Software and Code, J.C.; Manuscript editing, J.C.; Manuscript revision, W K. C. and H.T. Supervision, H.T.

428 Competing Interests

429 The authors declare no conflict of interest.

430 References

- 431 Bird, P.: An updated digital model of plate boundaries, *Geochemistry, Geophysics, Geosystems*, 4(3),
432 <https://doi.org/10.1029/2001GC000252>, 2003.
- 433 Bodri, B.: A neural-network model for earthquake occurrence, *Journal of Geodynamics*, 32(3), 289-310,
434 [https://doi.org/10.1016/S0264-3707\(01\)00039-4](https://doi.org/10.1016/S0264-3707(01)00039-4), 2001.
- 435 Cheng, D., Zhang, Y., and Wang, X.: Coseismic deformation and fault slip inversion of the 2017 Mw7.3
436 Halabjah, Iraq, earthquake based on Sentinel-1A data, *Acta Seismologica Sinica*, 41(4), 484-493,
437 <https://doi.org/10.11939/jass.20180113>, 2019.
- 438 Dieterich, J.: A constitutive law for rate of earthquake production and its application to earthquake
439 clustering, *Journal of Geophysical Research*, 99(B2), 2601, 1994.

440 Gu, J., Xie, X., and Zhao, L.: On temporal distribution of large aftershocks of the sequence of a major
441 earthquake and preliminary theoretical explanation, *Acta Geophysica Sinica*, 22(1), 32-46, 1979.

442 Han, Z.: Possible reduction of earthquake hazard on the Wellington Fault, New Zealand, after the nearby
443 1855, M8.2 Wairarapa earthquake and implication for interpreting paleoearthquake intervals, *Annals*
444 *of Geophysics*, 46(5), 1141-1154, <https://doi.org/10.4401/ag-3450>, 2003.

445 Harris, R. A.: Introduction to special section: stress triggers, stress shadows, and implications for seismic
446 hazard. *Journal of Geophysical Research*, 103(B10), 24347, <https://doi.org/10.1029/98JB01576>, 1998.

447 Jordan, MI., and Mitchell, T.M.: Machine learning: Trends, perspectives, and prospects, *Science*,
448 349(6245), 255-260, <https://doi.org/10.1126/science.aaa8415>, 2015.

449 Kagan, Y.Y., and Heidi, H.: Relation between mainshock rupture process and Omori's law for aftershock
450 moment release rate, *Geophysical Journal International*, 163(3), 1039-1048,
451 <https://doi.org/10.1111/j.1365-246X.2005.02772.x>, 2005.

452 Kagan, Y.Y., and Jackson, D.D.: Long-term probabilistic forecasting of earthquakes, *Journal of*
453 *Geophysical Research*, 99(B7), 13685-13700, 1994.

454 King, G.C.P., Stein, R.S., and Lin, J.: Static stress changes and the triggering of earthquakes, *Bulletin of the*
455 *Seismological Society of America*, 84(3), <https://doi.org/10.1029/94JB00611>, 1994.

456 Kong, Q., Trugman, D. T., and Ross, Z. E.: Machine Learning in Seismology: Turning Data into Insights,
457 *Seismological Research Letters*, 90(1), 3-14, <https://doi.org/10.1785/0220180259>, 2019.

458 Lecun, Y., Bengio, Y., and Hinton, G.: Deep learning, *Nature*, 521(7553), 436,
459 <https://doi.org/10.1038/nature14539>, 2015.

460 Lin, J.: Stress triggering in thrust and subduction earthquakes and stress interaction between the southern
461 San Andreas and nearby thrust and strike-slip faults, *Journal of Geophysical Research*,
462 109(B2),B02303, <https://doi.org/10.1029/2003jb002607>, 2004.

463 Lindman, M., Jonsdottir, K., and Roberts, R.: Earthquakes descaled: on waiting time distributions and
464 scaling laws, *Physical Review Letters*, 94(10), 108501,
465 <https://doi.org/10.1103/PhysRevLett.94.108501>, 2005.

466 Ma, K. F., Chan, C.H., and Stein, R.S.: Response of seismicity to Coulomb stress triggers and shadows of
467 the 1999 Mw=7.6 Chi-Chi, Taiwan, earthquake, *Journal of Geophysical Research Solid Earth*,
468 <https://doi.org/10.1029/2004JB003389>, 2005.

469 Meade, B. J., Devries, P. M. R., and Faller, J.: What Is Better Than Coulomb Failure Stress? A Ranking of
470 Scalar Static Stress Triggering Mechanisms from 105 Mainshock-Aftershock Pairs, *Geophysical*
471 *Research Letters*, 44, <https://doi.org/10.1002/2017GL075875>, 2017.

472 Mignan, A., and Broccardo, M.: A Deeper Look into 'Deep Learning of Aftershock Patterns Following
473 Large Earthquakes': Illustrating First Principles in Neural Network Physical Interpretability, *IWANN*
474 *2019: Advances in Computational Intelligence*, 3-14, https://doi.org/10.1007/978-3-030-20521-8_1,
475 2019.

476 Mogi, K.: On the time distribution of aftershocks accompanying the recent major earthquake in and near
477 Japan, *Bull Earthquake Res Inst*, 40:107-124, 1962.

478 Moustra, M., Avraamides, M., and Christodoulou, C.: Artificial neural networks for earthquake prediction
479 using time series magnitude data or seismic electric signals, *Expert Systems with Applications*,
480 38(12), 15032-15039, <https://doi.org/10.1016/j.eswa.2011.05.043>, 2011.

481 Nanjo, K. Z., Enescu, B., and Shcherbakov, R.: Decay of aftershock activity for Japanese earthquakes,
482 *Journal of Geophysical Research Solid Earth*, 112(B8), <https://doi.org/10.1029/2006JB004754>, 2007.

483 Narteau, C., Byrdina, S., and Shebalin, P.: Common dependence on stress for the two fundamental laws of
484 statistical seismology, *Nature*, 462(7273), 642-645, <https://doi.org/10.1038/nature08553>, 2009.

485 Narteau, C., Shebalin, P., and Holschneider, M.: Onset of power law aftershock decay rates in southern
486 California, *Geophysical Research Letters*, 32(22), L22312, <https://doi.org/10.1029/2005gl023951>,
487 2005.

488 Ogata, Y.: Statistical models for earthquake occurrences and residual analysis for point processes, *JASA*,
489 83(401), 9-27, 1988.

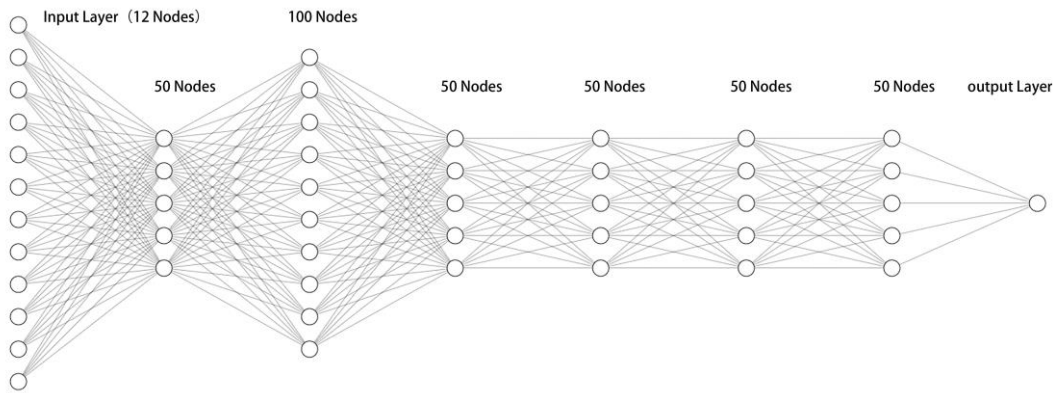
- 490 Ogata, Y.: Space-time point-process models for earthquake occurrences, *Annals of the Institute of*
491 *Statistical Mathematics*, 50(2), 379-402, 1998.
- 492 Okada, Y.: Surface deformation due to shear and tensile faults in a half-space, *Bull. Seismol. Soc. Amer.*,
493 75, 1135-1154, [https://doi.org/10.1016/0148-9062\(86\)90674-1](https://doi.org/10.1016/0148-9062(86)90674-1), 1985.
- 494 Okada, Y.: Internal deformation due to shear and tensile faults in a half-space, *Bull. Seismol. Soc. Amer.*,
495 82(2), 1018-1040, 1992.
- 496 Omori, F.: On aftershocks of earthquakes, *J. Coll. Sci. Imp. Univ. Tokyo*. 7, 11-200, 1894.
- 497 Phoebe, M. R. D., Fernanda, V., Martin, W. and Brendan, J. M.: Deep learning of aftershock patterns
498 following large earthquakes, *Nature*, 560(7720), 632-634, <https://doi.org/10.1038/s41586-018-0438-y>,
499 2018.
- 500 Scholz, C.H.: Microfracturing and the inelastic deformation of rock in compression, *Journal of Geophysical*
501 *Research*, 73(4), 1417-1432, <https://doi.org/10.1029/jb073i004p01417>, 1968.
- 502 Shan, X., Qu, C., and Gong, W.: Coseismic deformation field of the Jiuzhaigou Ms7.0 earthquake from
503 Sentinel-1A InSAR data and fault slip inversion, *Chinese Journal of Geophysics*, 60(12), 4527-4536,
504 <https://doi.org/10.6038/cjg20171201>, 2017.
- 505 Stein, R. S., and Lisowski, M.: The 1979 homestead valley earthquake sequence, California: control of
506 aftershocks and postseismic deformation, *Journal of Geophysical Research Solid Earth*, 88(B8),
507 <https://doi.org/10.1029/JB088iB08p06477>, 1983.
- 508 Steketee, J. A.: Some geophysical applications of the elasticity theory of dislocations. *Canadian Journal of*
509 *Physics*, 36(9), 1168-1198, <https://doi.org/10.1139/p58-123>, 1958.
- 510 Toda, S.: Toggling of seismicity by the 1997 Kagoshima earthquake couplet: A demonstration of time-
511 dependent stress transfer, *Journal of Geophysical Research*, 108(B12), 2567,
512 <https://doi.org/10.1029/2003jb002527>, 2003.
- 513 Utsu, T.: A statistic study on the occurrence of aftershocks, *Geophys*, 30, 521-545, 1961.
- 514 Utsu, T.: 43 Statistical features of seismicity, *International Geophysics*, 81, 719-732,
515 [https://doi.org/10.1016/S0074-6142\(02\)80246-7](https://doi.org/10.1016/S0074-6142(02)80246-7), 2002.
- 516 Wan, Y., Wu Z., and Zhou G.: Focal mechanism dependence of static stress triggering of earthquakes,
517 *Tectonophysics*, 390(1-4), 235-243, 2004.
- 518 Wang, Z., Zhang, R., and Wang, X.: InSAR coseismic deformation monitoring and fault inversion of 2016
519 Qinghai Menyuan Earthquake, *Remote Sensing Information*, 33(006), 103-108,
520 <https://doi.org/10.3969/j.issn.1000-3177.2018.06.015>, 2018.
- 521 Wong, K., and Schoenberg, F. P.: On mainshock focal mechanisms and the spatial distribution of
522 aftershocks, *Bulletin of the Seismological Society of America*, 99(6), 3402-3412, 2009.
- 523 Yang, Z., Chen, Y., and Zheng, Y.: The application of double differential seismic location method in the
524 accurate location of earthquakes in central and western China, *Science in China(Series D)*, 33(z1),
525 <https://doi.org/10.1360/03dz0014>, 2003.
- 526 Yi, G., Wen, X., and Xin, H.: Distributions of seismicity parameters and seismic apparent stresses on the
527 Longmenshan-Minshan tectonic zone before the 2008 Ms8.0 Wenchuan earthquake, *Acta Geophysica*
528 *Sinica*, 54(006), 1490-1500, <https://doi.org/10.3969/j.issn.0001-5733.2011.06.008>, 2011.
- 529 Zhu, H, and Wen, X.: Stress triggering process if the 1973 to 1976 Songpan, Sichuan, sequence of strong
530 earthquake, *Chinese J. Geophys*, 52(4), 994-1003, <https://doi.org/10.3969/j.issn.0001-5733.2009.04.016>, 2009.
- 531
- 532 Zhao, J.: Application of InSAR technology in surface deformation monitoring, M.S. thesis, Nanjing
533 University, China, 2019.
- 534 Zhao, Z., and Chen, N.: Accuracy amendment of focal location along the Longmenshan fault in the north of
535 Sichuan, *Earthquake Research in Sichuan*, 4, 19-30, 1995.

536
537
538
539

540
541
542
543
544
545
546

547 **Figure**

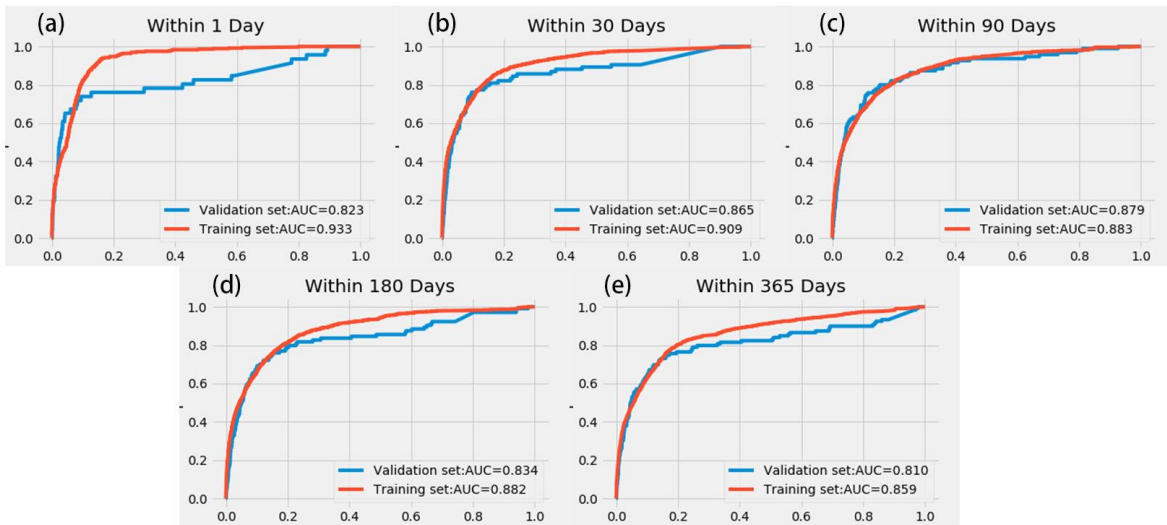
548



549
550

551 **Figure 1.** The structure of **DNN**. The neural network is composed of an input layer, hidden layers, output
552 layers and the connections between each layer. The function of each hidden layer is to transform the
553 features of the network input.

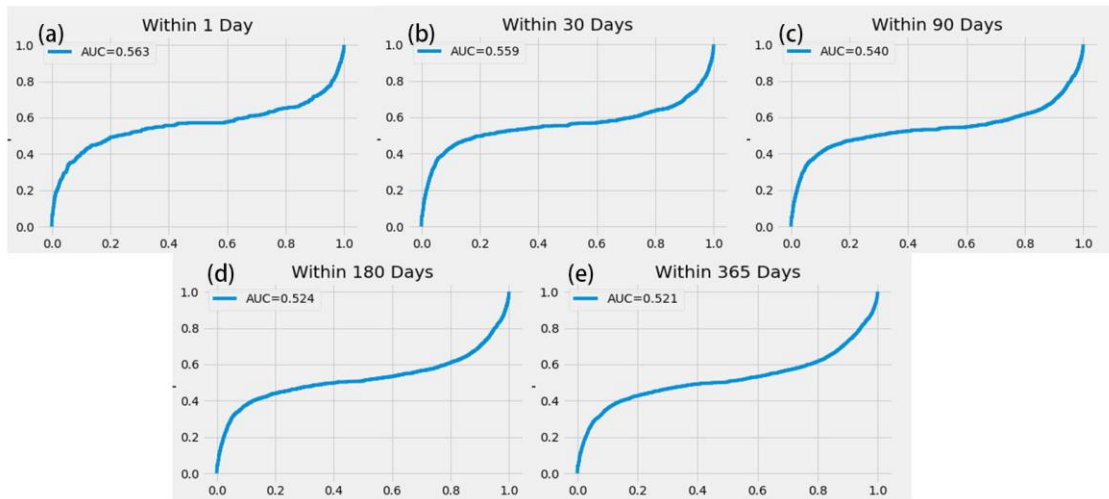
554



555
556

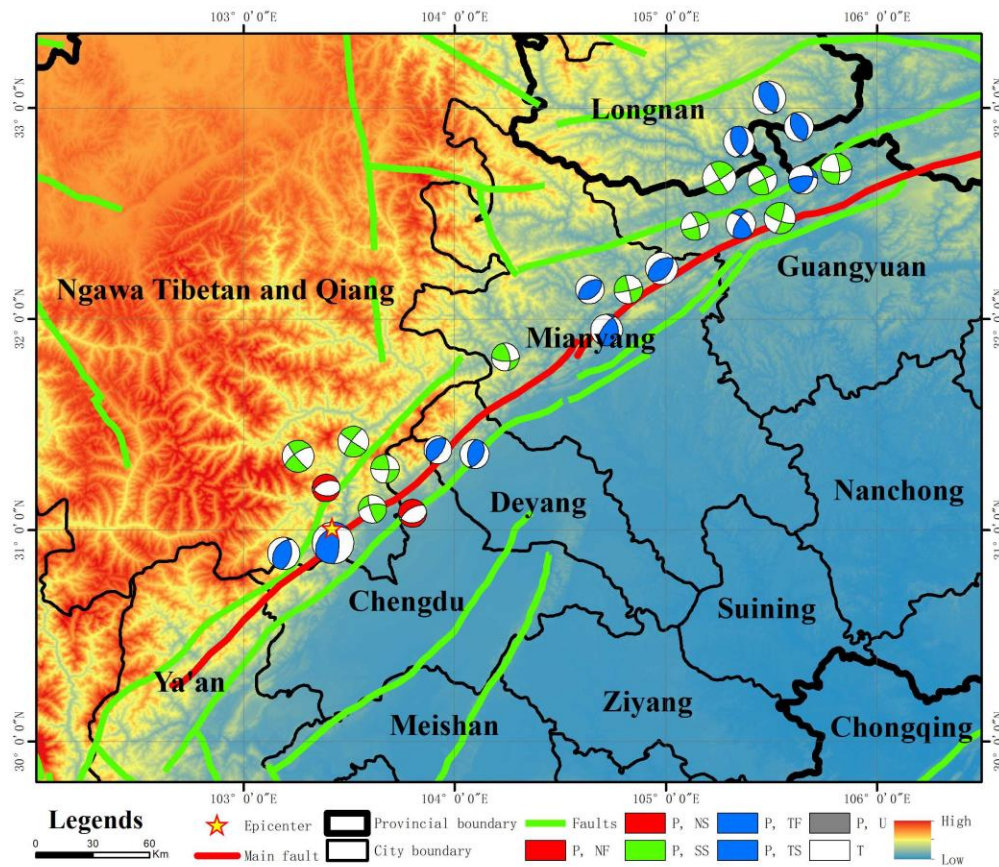
557 **Figure 2.** ROC curve for multiple time scales. Figures (a) through (e) show the ROC curve of the model
558 within 1 d, 30 d, 90 d, 180 d and 365 d, respectively. The horizontal axis represents the FPR (false positive
559 rate) and the vertical axis represents the TPR (true positive rate).

560



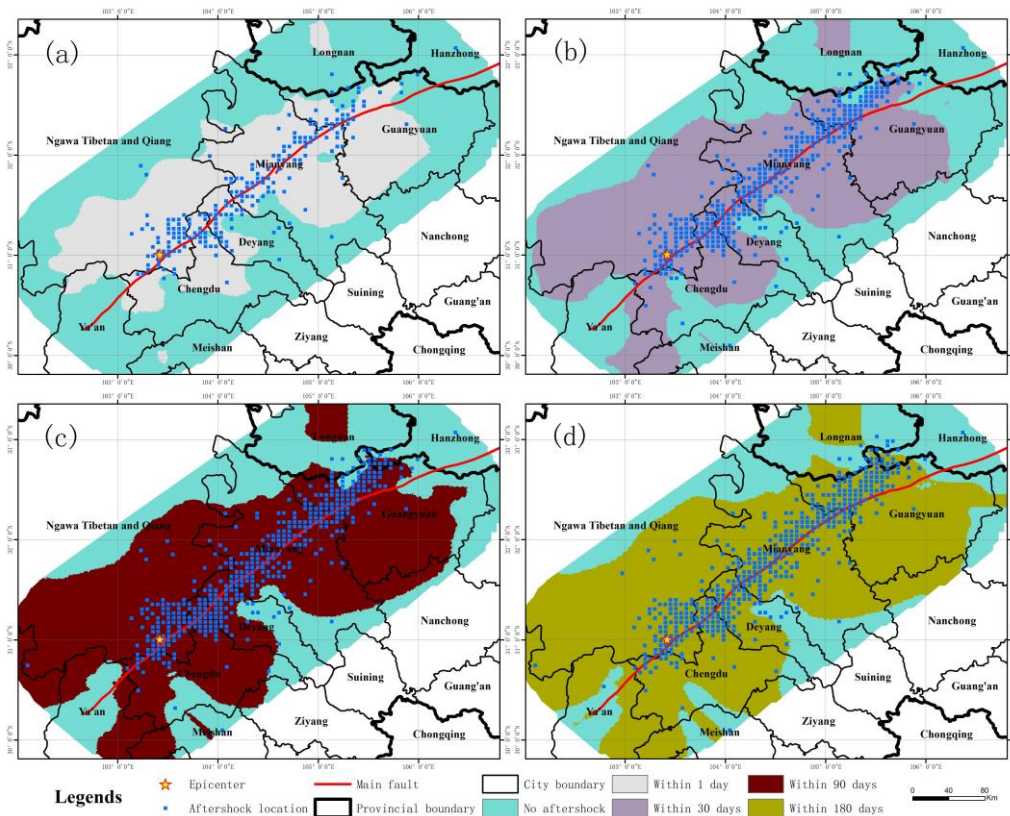
561
562
563
564
565
566

Figure 3. ROC curve of ΔCFS for multiple time scales. Figures (a) through (e) show the ROC curve of the model within 1 d, 30 d, 90 d, 180 d and 365 d, respectively. The horizontal axis represents the FPR (false positive rate) and the vertical axis represents the TPR (true positive rate).



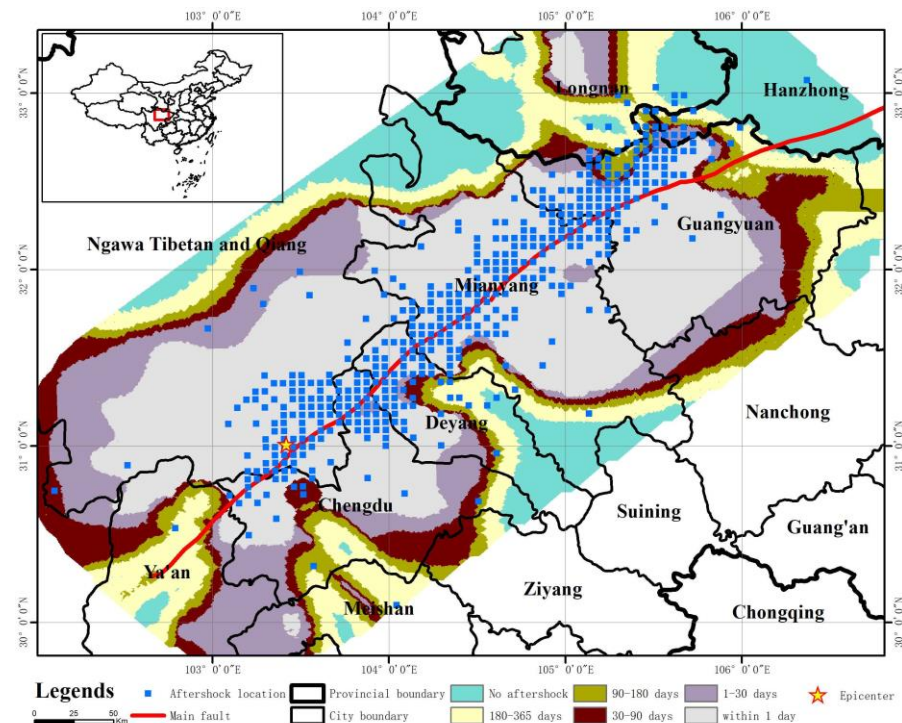
567
568
569
570
571
572
573
574

Figure 4. Structural background map of the Wenchuan earthquake. The red line and green line represent the fault structures in this area. The red line is the main fault zone of the Wenchuan earthquake, and the green line represents other fault zones. The ellipsoid of the focal mechanism of the main aftershocks is shown, which represents the types of reverse faults: strike slip reverse fault, normal fault, strike slip normal fault and strike slip fault.



575
576
577
578
579
580

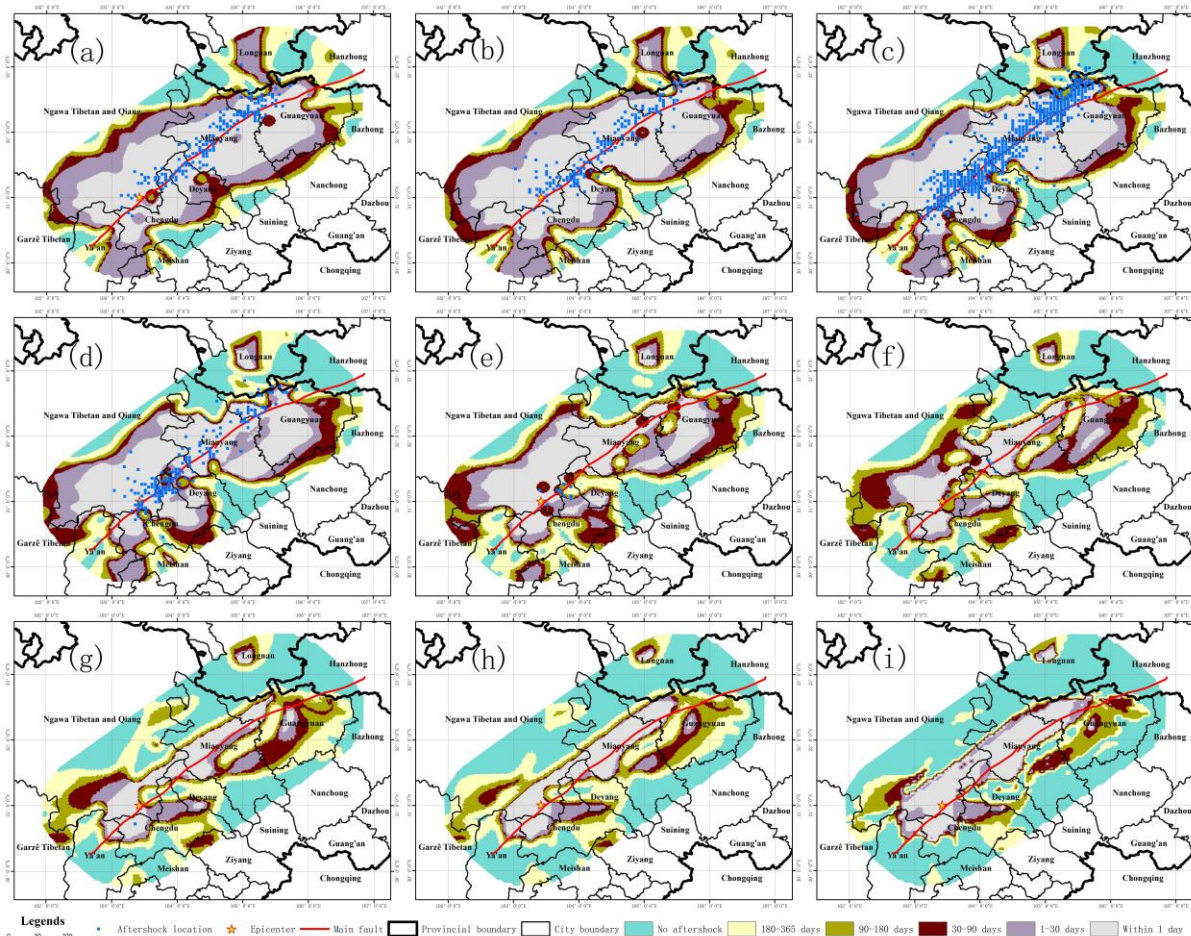
Figure 5. Aftershock damage patterns of the Wenchuan earthquake at multiple time scales. Figures (a) through (d) show the aftershock damage pattern within 1 d, 30 d, 90 d and 180 d, respectively. The blue dots indicate the actual location of aftershocks at the corresponding time scale.



581
582

583 **Figure 6.** Aftershock hysteresis effect of the Wenchuan earthquake. The aftershock hysteresis effect can be
584 observed by combining the aftershock patterns of the Wenchuan earthquake at different time scales. The
585 blue dots indicate the locations of the actual aftershocks over one year.

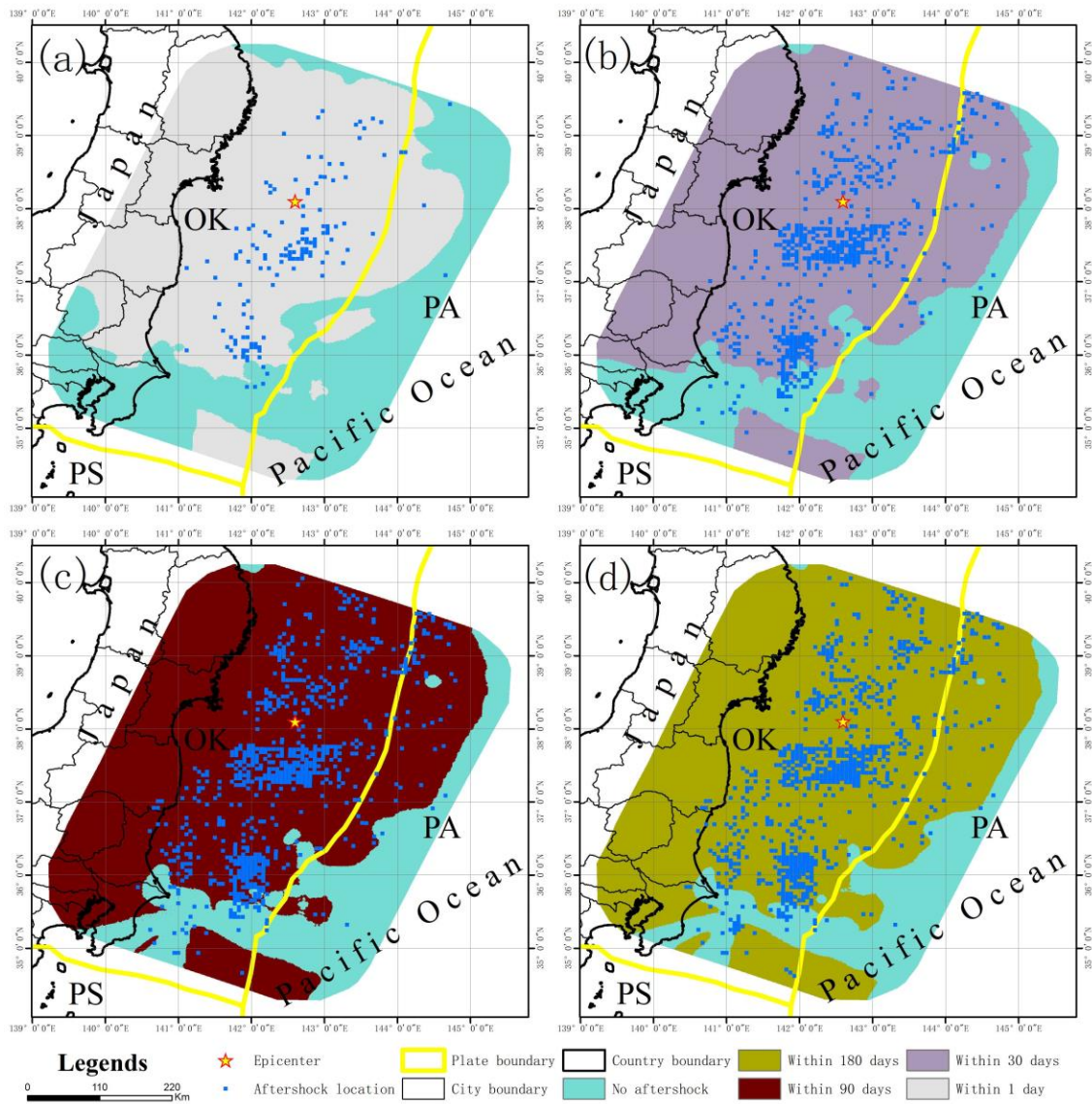
586



587
588

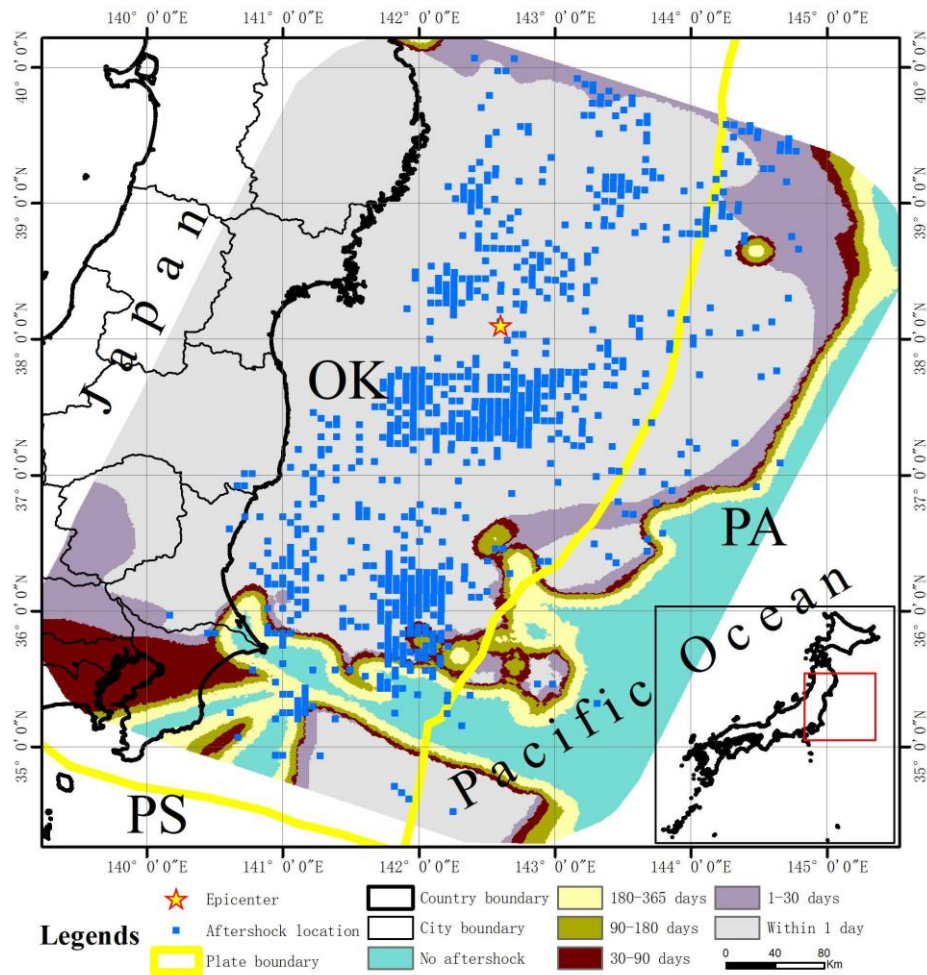
589 **Figure 7.** Aftershock hysteresis effect of the Wenchuan earthquake in different depths. Figures (a) through
590 (i) show the aftershock hysteresis effect of the Wenchuan earthquake for depth sections of 2,500 m, 7,500
591 m, 12,500 m, 17,500 m, 22,500 m, 27,500 m, 32,500 m, 37,500 m, and 42,500 m, respectively.





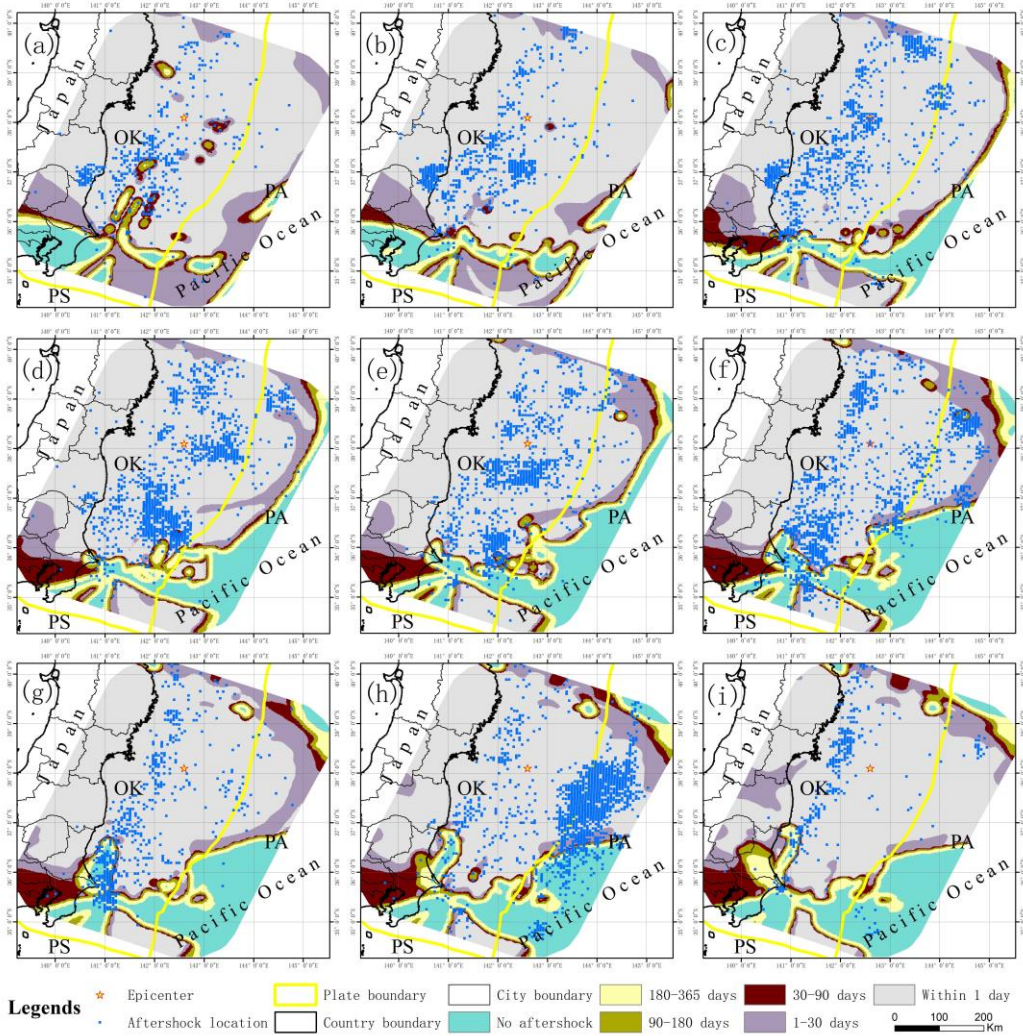
592
593

594 **Figure 8.** Aftershock damage patterns of the Tohoku earthquake at multiple time scales. Figures (a)
595 through (d) show the aftershock damage pattern of the Tohoku earthquake within 1 d, 30 d, 90 d and 180 d,
596 respectively. The blue dots indicate the actual location of aftershocks at the corresponding time scale.



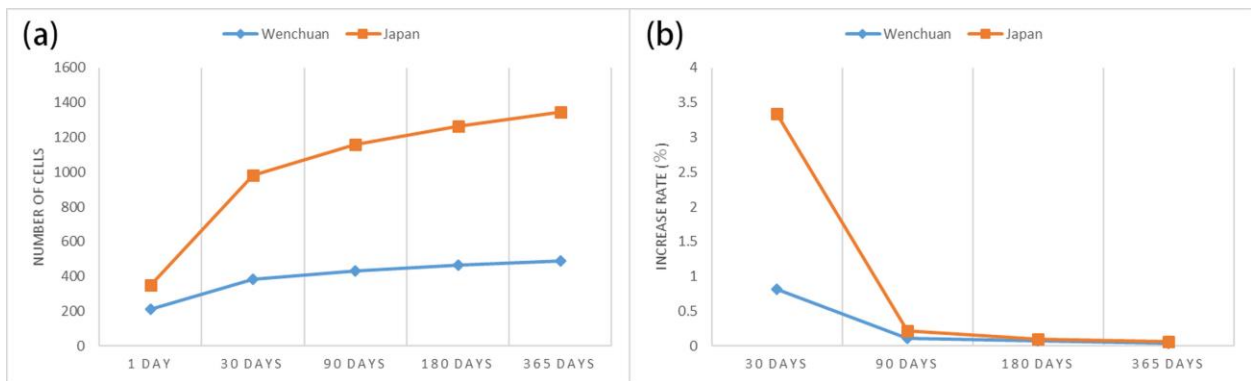
597
598

599 **Figure 9.** Aftershock hysteresis effect of the Tohoku earthquake in Japan. The aftershock hysteresis effect
600 can be observed by combining the aftershock patterns of the Tohoku earthquake at different time scales.
601 The blue dots indicate the locations of the actual aftershocks over one year.



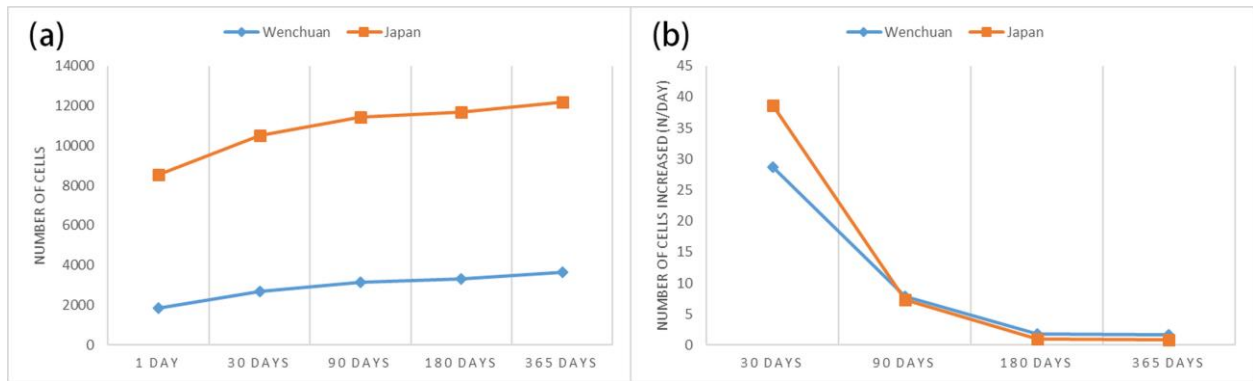
602
603
604
605
606
607
608
609

Figure 10. Aftershock hysteresis effect of the Tohoku earthquake at different depths. Figures (a) through (i) show the aftershock hysteresis effect of the Tohoku earthquake for depth sections of 2,500 m, 7,500 m, 12,500 m, 17,500 m, 22,500 m, 27,500 m, 32,500 m, 37,500 m, and 42,500 m, respectively.



610
611

612 **Figure 11.** The curve of aftershock hysteresis effect (actual aftershocks). Figure (a) shows the change in
613 the number of cells with aftershocks at different time scales, and figure (b) shows the change in the growth
614 rate of the number of cells with aftershocks at different time scales.
615



616
617
618 **Figure 12.** The curve of aftershock hysteresis effect (predicted aftershock pattern). Figure (a) shows the
619 number of cells with aftershocks predicted at different time scales, and figure (b) shows the increment of
620 cells with aftershocks at each time scale.
621